Journal Name

RSCPublishing

ARTICLE

Cite this: DOI: 10.1039/xoxx00000x

Received ,
Accepted

DOI: 10.1039/xoxx00000x

www.rsc.org/

The nature of chemical bonding in actinide and lanthanide ferrocyanides determined by X-ray absorption spectroscopy and density functional theory

Thomas Dumas[a], Dominique Guillaumont[a], Clara Fillaux[a], Andreas Scheinost[b], Philippe Moisy[a], Sébastien Petit[a], David K. Shuh[c], Tolek Tyliszczak[d], Christophe Den Auwer[a,e]

The electronic properties of actinide cations are of fundamental interest to describe intramolecular interactions and chemical bonding in the contexts of nuclear waste reprocessing or direct storage. The 5f and 6d orbitals are the first partially or totally vacant states in these elements, and the nature of the actinide ligand bonds is related to their ability to overlap with ligand orbitals. Because of its chemical and orbital selectivities, X-ray absorption spectroscopy (XAS) is an effective probe of actinide species frontier orbitals and for understanding actinide cation reactivity toward chelating ligands. The soft X-ray probes of the light elements provide better resolution than actinide L_3-edges to obtain electronic information from the ligand. Thus coupling simulations to experimental soft X-ray spectra measurements and complementary quantum chemical calculations yields quantitative information on chemical bonding. In this study, soft X-ray XAS at the K-edges of C, N, and the $L_{2,3}$-edges of Fe was used to investigate the electronic structures of the well-known ferrocyanide complexes $K_4Fe^{II}(CN)_6$, thorium hexacyanoferrate $Th^{IV}Fe^{II}(CN)_6$, and neodymium hexacyanoferrate $KNd^{III}Fe^{II}(CN)_6$. The soft X-ray spectra were simulated based on quantum chemical calculations. Our results highlight the orbital overlapping effects and atomic effective charges in the $Fe^{II}(CN)_6$ building block. In addition to providing a detailed description of the electronic structure of the ferrocyanide complex ($K_4Fe^{II}(CN)_6$), the results strongly contribute to confirming the actinide 5*f* and 6*d* orbital oddity in comparison to lanthanide 4*f* and 5*d*.

Introduction

Ever since the second half of the 20th century, there has been increasing interest in the actinide elements and a growth in their strategic significance. From a fundamental point of view, our understanding of the physical chemistry of the actinides, although extensively explored for over a century, still lags compared to that of most elements in the periodic table. For instance, the ability of actinide species to form covalent bonds and the relative role of 5*f* and 6*d* orbital contributions is still a subject of investigation. Over the past few decades, transition elements have been widely studied to unravel the nature of bonding in molecular inorganic systems. The 3*d*, 4*d*, and 5*d* metal interactions with common ligands are now well-described and the covalent contributions to bonding resulting from the overlap of the extended and valence orbitals with orbitals from ligands has been recognized. Lanthanide and actinide families result from the insertion of *f*–type orbitals within the electronic configuration of the transition metal block, whose chemistry is largely governed by its *d* orbitals. Unlike the *d* orbitals, the 4*f* orbitals of the lanthanide family are known to be strongly localized. Consequently, lanthanide interactions with organic ligands are considered to be mostly ionic[1]. The actinide family is often schematically described as behaving with intermediate properties. The involvement of 5*f* and 6*d* orbitals in covalent bonding with ligands was under debate at the beginning of actinide science[2,3].

This is particularly true for the early actinides, which are more versatile in terms of oxidation states than the heavier actinides as well as the lanthanides. Actinide 5*f* and 6*d* electronic states have a wider radial distribution[4] than lanthanide 4*f* and 5*d* states, due to the combined effect of an increase in principal quantum number for d and f orbitals (from n = 5 to 6 and from n = 4 to 5 respectively) and the indirect relativistic effect. It is therefore reasonable to believe that the 5*f*-6*d* ability to overlap with ligand orbitals is favored compared to the 4*f*-5*d* interaction. The formation of actinyl *trans*-oxocations is the most relevant experimental evidence of covalent effects in actinide bonding involving *f*-orbitals (U-O distance in UO_2^{2+} is 1.7-1.8 Å in aqueous media[5] because of the oxygen $2p_{x,y,z}$ orbital overlap with uranium $6d_{xz,yz,z2}$ and $5f_{xz2,\ yz2,z3}$[6]). For +III and +IV oxidation states, the role of 5*f* and 6*d* orbitals in covalent bonding is harder to define. A strategy to unravel the role of 5*f*-6*d* orbitals in putative covalent bonding consists in fostering the orbital overlap by the use of soft (polarizable) ligands (see Brennan *et al.* [7],

Karamazin *et al*[8] and Mazzanti et *al*[9]). In such cases, the decrease of the actinide-ligand distances compared to those of the lanthanide-ligands is taken as indirect evidence (although neither unique nor definitive) of a covalent effect. There is also evidence, from a theoretical point of view, that relatively soft ligands promote the orbital overlap with actinides, whereas they have a lesser influence on lanthanides[10,11]. Nowadays, modern computational techniques based on topological electronic analyses are more confident in assigning a covalent character in actinide ligand bonds[12,13,14]. Covalent effects in actinide complexes were for instance investigated by Kozimor et *al*. using X-ray absorption spectroscopy (XAS) at chlorine K edge and compared to transition metals in a series of $(C_5Me_5)_2MCl_2$ complexes (M= Ti, Zr, Hf, Th, U)[15]. Following the same methodology, the study of Minasian et al.[16] combined XAS measurements and time-dependent density functional (TDDFT) calculations. In recent papers, Minasian[17] showed evidence of metal–carbon orbital mixing in thorocene and uranocene, combining DFT calculations and carbon K-edge XAS spectra and covalency in lanthanide chlorine bonds was investigated by Loble[18]. More generally in coordination chemistry, the strategy based on the use of XAS as a probe to estimate covalency has been extensively described, and has been compared to theoretical calculations in the literature[19-21]. For instance, soft XAS has already been applied by Hocking *et al*. [22] to describe the electronic structure of ferrocyanide complexes as well as the cyano-bridged Prussian Blue family[23-25].

The work presented here is part of a program to explore the actinide hexacyanoferrate family from both structural and electronic perspectives. We have extended our previous structural investigations of early actinide hexacyanoferrate compounds to probe covalent effects in an actinide–cyano bond. The electronic structure of the hexacyanoferrate family was first described by Robin and Day[26]. Because of the intermetallic charge transfer process along the cyano bridge, *d* element Prussian Blue analogs are characterized by a large covalency within ligand-metal bonds along this bridge[27,28]. Comparison with actinide analogs is expected to shed light on the covalent character in actinide hexacyanoferrates. Two of our recent papers have shown that actinide (Th-Am) ferrocyanide complexes[29,30] are isostructural with the early lanthanide (La-Nd) ferrocyanide complexes (La-Nd). This report focuses on the use of soft XAS to compare the electronic structure of the potassium ferrocyanide (**$K_4[Fe^{II}(CN)_6]$**) compound to the actinide and lanthanide ferrocyanide compounds $KNdFe^{II}(CN)_6{,}4H_2O$ and $ThFe^{II}(CN)_6{,}5H_2O$ (designated as **Nd^{III}/Fe^{II}** and **Th^{IV}/Fe^{II}** hereafter). Iron, carbon, and nitrogen soft X-ray near-edge absorption (NEXAFS) spectra were recorded to elucidate the electronic structure in Fe-C-N-Th/Nd bonds and are further compared to the non-bridging ferrocyanide reference, **$K_4[Fe^{II}(CN)_6]$**. In addition to a qualitative description of the NEXAFS spectra, a DFT–based approach similar to that used by Fillaux[31,32] has been implemented. With such a strategy, a semi quantitative interpretation of actinide-ligand bonding is proposed through the formation of Th*5f*/CNπ* molecular orbitals.

A Materials and Method

a Synthesis

All syntheses were described in a previous report[29] and the same materials were used for these studies.

b STXM data acquisition and processing

X-ray absorption spectra were obtained at the Molecular Environmental Science Beamline 11.0.2 scanning transmission X-ray microscope (STXM) at the Advanced Light Source (ALS-MES), Lawrence Berkeley National Laboratory, U.S.A.[33]. Soft X-ray STXM is well–suited to the investigation of actinides and radioactive materials, since the amount of material required is very small. It offers the opportunity to investigate radioactive samples in an efficient and safe way. In our experiments, the sample was finely ground in a fume hood dedicated to radiological use and the particles transferred to a 50 nm thick silicon nitride window (1 mm square). A second 50 nm window was glued onto the first and the double window sample package checked to ensure there was no residual contamination. The available energy range was approximately 100 eV–2000 eV and the energy resolution of the measurements was better than 0.1 eV at light element K-edges (C, N, O). The XAS spectrum acquisition was performed by using the STAKS procedure implemented in aXis 2000[34].

c DFT calculations

Electronic structure calculations were performed on model molecular compounds in their ground state to (i) obtain a detailed electronic structure to help near edge X-ray absorption fine structure (NEAFS) spectra interpretation, and (ii) improve the NEXAFS simulation using the calculated electronic population as an input in the simulation. Both **$K_4Fe(CN)_6$** and **Th^{IV}/Fe^{II}** systems are periodic and cannot be handled ideally with the calculation methods chosen. For **$K_4Fe(CN)_6$** different molecular models were tested to take into account the potassium atoms and waters of hydration. The electronic structure of **$K_4Fe(CN)_6$** has been widely investigated using theoretical techniques. Hocking et al. [22] and Ryde et al. [35] studied charged octahedron $Fe(CN)_6^{4-}$ clusters with DFT/BPP6. Here, a neutral $K_4\{Fe(CN)_6\}$ cluster with four K^+ cations in tetrahedral positions was selected (**Figure. 1a**). **Th^{IV}/Fe^{II}** has both Fe-CN and Th-CN bonds, and thus the geometry chosen (**Figure. 1b**) was adopted taking into account the following points:

- The cluster had to be centered on the $Fe(CN)_6$ unit to be consistent with $K_4[Fe(CN)_6]$ calculations. Thorium atoms were added to form 6 equivalent cyano bridges.
- The geometry was frozen at the bond distances and angles determined previously from extended X-ray absorption fine structure study.
- The first thorium coordination shell (N, O) was completed with partial charges to limit the unrealistic charge effect around the Th^{4+} cation and to establish a neutral cluster.

To determine the electronic structure in the ground state, DFT calculations were performed with the ADF package[36] . Relativistic effects were taken into account using the Zero Order Regular Approximation ("ZORA")[37]. The unrestricted approach was used and spin-orbit effects were not taken into account. The BP86 functional and atomic basis of Slater function triple-zeta (TZ2P) were used. Charges and electronic populations were determined by Mulliken and natural population analysis (NPA) analyses[38]. Because of the strong electronic delocalisation along the cyano ligand, this DFT based methodology was only applicable to the close shell thorium system. For this reason, the methodology was not applied to **Nd^{III}/Fe^{II}**.

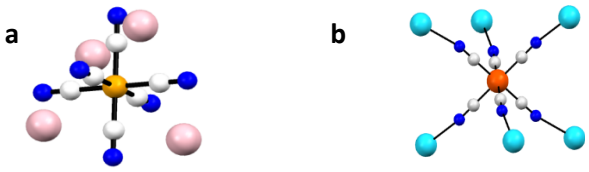

Fig. 1: **a)** $K_4Fe(CN)_6$ cluster. **b)** $Fe\text{-}(\mu CN)_6\text{-}Th_6\text{-}\delta^-_x$.cluster. *Iron - orange, carbon - white, nitrogen - blue, potassium - pink and thorium - light blue* (partial charges are not shown).

d XAS spectrum simulation

Two types of simulation approaches are used to describe the final state, depending on the orbitals involved in the X-ray absorption process:

- When the states probed are d orbitals, a multielectronic approach based on multiplet theory must be used. Iron $L_{2,3}$-edges in ferrocyanide complexes and in analogous Prussian blue 3d compounds[39,40] have been simulated in this manner.
- When the states probed are 2*p* orbitals, multielectronic effects can be ignored and a monoelectronic approach is used. For the cyano ligand, hybridized 2*p* orbitals are diffuse and very sensitive to geometry (distances, symmetry) and charge transfer (LMCT or

MLCT). To simulate the C and N K-edges, partial atomic charges are needed and preliminary DFT calculations are therefore essential. We selected the FDMNES code for K-edge simulations. This code is described in the literature[41] and the methodology has already been applied to actinide compounds[31,37,38]. The FDMNES program may be used in two different modes for the calculation of potentials: the Green formalism with a muffin-tin approximation and the Finite Difference Method (FDM). The FDM method avoids spherical muffin-tin shaped atomic potentials. A schematic description of the methodology selected is given in **SI.2**. To validate this monoelectronic approach, the carbon K-edge spectrum of **$K_4[Fe(CN)_6]$** was used as a reference to test the different procedures. The first attempt, using muffin-tin potentials (**SI. 3**) did not give satisfactory agreement with the experimental data. Although more time-consuming, the FDM was therefore employed. Moreover, simulations were systematically performed using 3 different electronic configurations: (i) neutral charges, (ii) Mulliken electronic populations from the DFT, and (iii) NPA electronic population also derived from DFT (**Table 2**). Fillaux *and al*. demonstrated the utility and advantage of using the Mulliken charges for actinides in the FDMNES program. The improved accuracy of the simulated spectra based on the Mulliken electronic populations confirmed this result (**Figure 3b**). Furthermore, the simulated features were convoluted with a Lorentzian function to take into account the core-hole lifetime.

B Results

a XAS (nitrogen and carbon K-edges, iron $L_{2,3}$-edges)

In the dipole approximation, carbon and nitrogen K-edge absorption spectra correspond to electronic transitions from the nitrogen or carbon *1s* atomic orbital to vacant 2*p* orbitals, and(or) to any orbital available possessing *p* character in a vacant MO. In the cyano ligand, the nitrogen and carbon K-edges probe the same antibonding cyano π* orbitals (see molecular orbital diagrams calculated by DFT for CN^- ligand **SI3**). Additional bonding information is also available from iron $L_{2,3}$-edges. Iron $L_{2,3}$-edge spectra correspond to transitions to vacant *3d* orbitals or to unfilled MOs with a *d* character. A first quantitative interpretation of the nitrogen and carbon K-edge spectra, as well as the iron $L_{2,3}$-edge spectra, is given hereafter. Because cyano ligands in **$K_4Fe(CN)_6$**, **Th^{IV}/Fe^{II}** and **Nd^{III}/Fe^{II}** are structurally equivalent and no other nitrogen and carbon atoms are present in the structure, the direct interpretation of the carbon and nitrogen K-edge spectra is simplified. The spectra obtained for **$K_4Fe(CN)_6$**, **Th^{IV}/Fe^{II}** , and **Nd^{III}/Fe^{II}** are presented in **Figures 2a-b** for carbon and nitrogen, respectively. At first glance both series of edges show a similar evolution over the carbon and nitrogen K-edges. It is interesting to note that the K-edge transitions (formally $1s^2 2p^n \rightarrow 1s^1 2p^{n+1}$) of C and N are quite similar because the final state MOs are the same cyano π* and are only little altered from their atomic character. Consequently, the evolution observed for the two series resulting from changes in the π* probed are consistent at both C and N edges. A single peak (peak **A**) can be observed for **$K_4Fe(CN)_6$** with a maximum at 399.8 eV and 286.5 eV for the nitrogen and carbon edges, respectively. For **Nd^{III}/Fe^{II}**, peak **A** is slightly shifted (399.6 eV and 286.2 eV, respectively) and a weak second feature (peak **a**) arises at higher energy (Δ_{Aa}=1.5 eV). For the **Th^{IV}/Fe^{II}** compound, peak **A** is again shifted (399.6 eV and 286.2 eV, respectively) and a more intense second peak (peak **B**) is observed at higher energy (Δ_{AB}=2.2 eV). The iron $L_{2,3}$-edge spectra of **$K_4Fe(CN)_6$**, **Nd^{III}/Fe^{II}**, and **Th^{IV}/Fe^{II}** are shown in **Figure 2c**. The experimental spectrum of **$K_4Fe(CN)_6$** is identical to that previously published by Hocking**Error! Bookmark not defined.**. Two peaks (**C** and **D)** appear at both L_2- and L_3-edges. The splitting of the 2p→3d transition is attributed to the crystal field splitting and cyano-iron π back-bonding effect. The first peak **C** corresponds to transitions to the two e_g* MOs, whereas the second transition **D** is attributed to transitions to the three t_{2g}* MOs (see Molecular orbital diagram, Figure 3a). In terms of edge position, peak **C** is shifted from 710.0 eV (**$K_4Fe(CN)_6$**) to 710.2 eV for **Nd^{III}/Fe^{II}**, and to 710.3 eV for **Th^{IV}/Fe^{II}**.

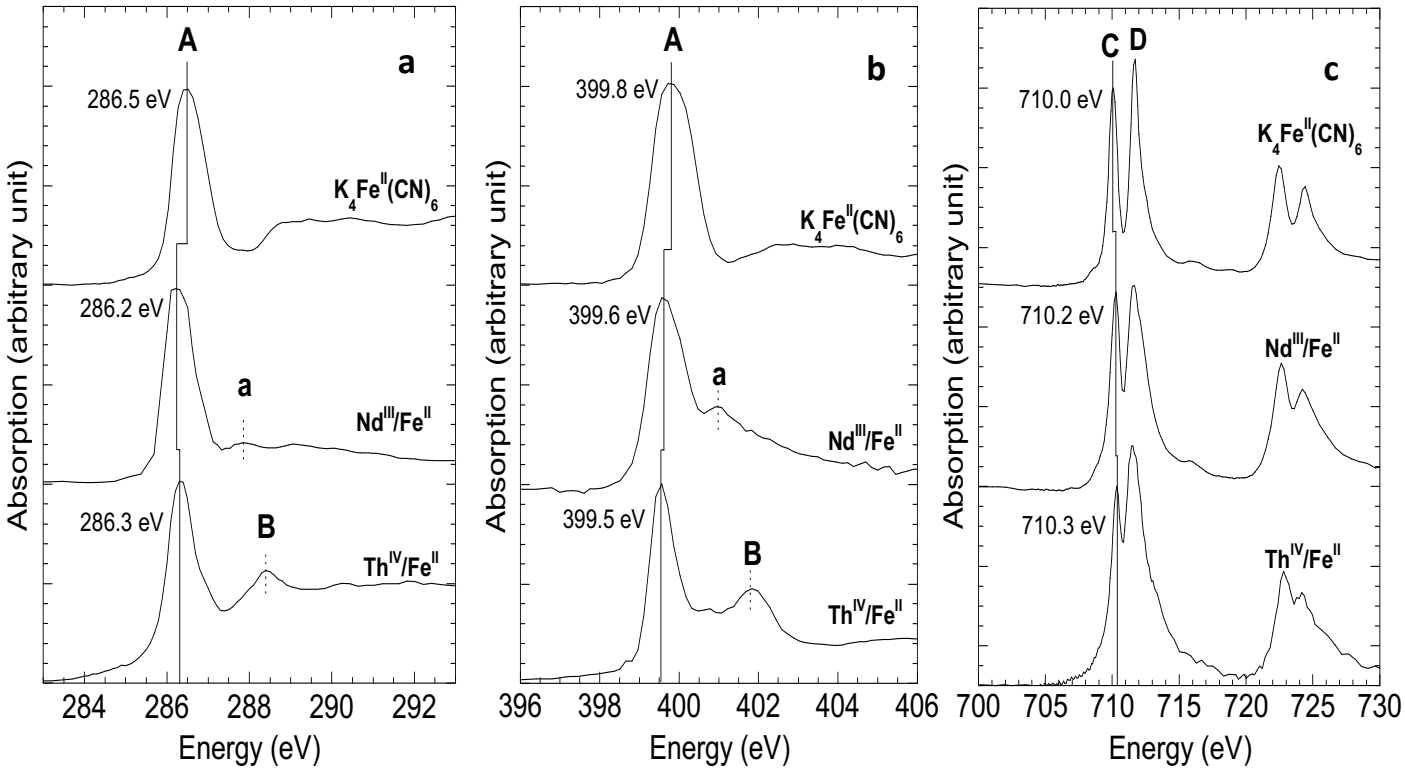

Figure 2 : **a)** Carbon K-edges of **$K_4Fe(CN)_6$**, **Nd^{III}/Fe^{II}**) and **Th^{IV}/Fe^{II}**. **b)** Nitrogen K-edges of **$K_4Fe(CN)_6$**, **Nd^{III}/Fe^{II}**) and **Th^{IV}/Fe^{II}**. **c)** Iron $L_{2,3}$-edges of **$K_4Fe(CN)_6$**, **Nd^{III}/Fe^{II}**) and **Th^{IV}/Fe^{II}**.

Peaks **C** and **D** observed in the $\mathbf{Nd^{III}/Fe^{II}}$ and $\mathbf{Th^{IV}/Fe^{II}}$ spectra are slightly different from those of $\mathbf{K_4Fe(CN)_6}$. Peak **D** broadening for the $\mathbf{Nd^{III}/Fe^{II}}$ and $\mathbf{Th^{IV}/Fe^{II}}$ suggests changes in the iron-cyano MLCT and LMCT similar to *d* block Prussian blue analogs reported by Bonhommeau[40]. Interpretation and further simulation of these L-edges is complicated by the necessity to take into account the multielectronic effects. Furthermore, in the case of $\mathbf{Th^{IV}/Fe^{II}}$, the thorium N_4-edge appears at 712 eV and overlaps into the iron L_3-edge region. This coincidence makes it difficult to simulate and meaningfully interpret the Fe and Th spectra. For instance, the higher intensity observed for $\mathbf{Th^{IV}/Fe^{II}}$ peak **D** is an artefact attributable to additional absorption of the thorium N_4-edge and is not indicative of any changes in the electronic structure.

b DFT calculation (description of MO systems)

Our strategy was to compare the calculated ground state electronic structure to the experimental XAS features, or in other words, to map the MOs involved in the XAS spectra of $\mathbf{Th^{IV}/Fe^{II}}$ and $\mathbf{K_4Fe(CN)_6}$ (partially or totally unoccupied *p* or *d* MOs).

$K_4Fe(CN)_6$:

Figure 3a presents the MO interaction diagram of 6 CN^- fragments with the Fe^{2+} cation and four K^+ (as described previously). As previously described for $\{Fe(CN)_6^{4-}\}$, a typical MO diagram representative of a $3d^6$ configuration transition metal in an octahedral ligand field with σ donor / π acceptor ligand was obtained. The five iron 3*d* orbitals are split into two occupied/unoccupied e_g/e_g^* and three t_{2g}/t_{2g}^* MOs. The e_g MOs result from the σ interaction between Fe-d_{z^2}, Fe-$d_{x^2-y^2}$ and cyano-5σ, whereas the t_{2g} MOs result from the π back-bonding interaction between Fe-d_{xy}, Fe-d_{xz} and Fe-d_{yz} with 3 cyano-π* orbitals. The other 9 cyano π* MOs remain almost unchanged.

The corresponding $\mathbf{K_4[Fe(CN)_6]}$ MO compositions are reported in **Table 1**. The contributions of the cyano σ orbitals to the two e_g and e_g^* MOs are 82% and 48% respectively. Charge transfer can be observed between the iron and cyano ligands. **Table 2** presents the calculated atomic charges and electronic populations, obtained by Mulliken and NBO analyses. The unexpected negative value on iron is due to the overestimated value obtained for the extended 4s and 4p iron orbitals (MULLIKEN gives, for instance, respectively 0.21 and 2.21 instead of 0).

Fe-(μCN)$_6$-Th$_6$-δ^-_x:

The MO diagram of $\mathbf{Fe\text{-}(\mu CN)_6\text{-}Th_6\text{-}\delta^-_x}$ is given in **Figure 3b**, and the composition of the main MOs involved in the XAS process are presented in **Table 1** for comparison with $K_4[Fe(CN)_6]$. The charge analyses as well as the electronic populations are compared to those of $\mathbf{K_4[Fe(CN)_6]}$ in **Table 2**. As for $\mathbf{K_4Fe(CN)_6}$, the iron 3d orbitals remain split into two main groups. In **Figure 3**, the Fe 3d e_g, e_g^*, t_{2g}, and t_{2g}^* orbital splitting in O_h symmetry can be observed. Even so, the t_{2g} orbital group is not fully degenerated (0.1 eV split) because of the imperfect O_h position for the six thorium atoms. For clarity and easier comparison with $\mathbf{K_4Fe(CN)_6}$, the O_h group labels e_g and t_{2g} are maintained in the following of the discussion.

The nine nonbonding π* orbitals observed in $\mathbf{K_4Fe(CN)_6}$ are here further split by the additional Th-NC interaction. The cyano π* MOs can be divided into two groups separated by 1.6 eV (indicated as $\Delta_{CN\pi^*}$ in **Figure 3b**). The thorium *5f* atomic orbitals (in green, **Figure 3b**) are also split by the cyano ligand field (equal to 0.82 eV) as well as the *6d* (in violet, **Figure 2b**) by 5.30 eV. Finally, the thorium *7s* orbitals remain unaffected. Again, to clarify notation and because $\mathbf{Fe\text{-}(\mu CN)_6\text{-}Th_6\text{-}\delta^-_x}$ is formally a D_{3d} symmetry cluster, MOs containing Th *f* or *d* characters will be named after the OAs from which they originate, instead of their symmetry labels. **Table 1** provides additional information about the effect of thorium on ferrocyanide orbital mixing. Thorium affects both the π* back-bonding and σ bonding in $\{Fe(CN)_6\}$ by Th *6d* and *5f* AOs orbital mixing in the formal $\{Fe(CN)_6\}$ e_g^*, t_{2g}, and t_{2g}^* MOs. Consequently, the Fe-*3d* contribution decreases slightly from 72% to 67% for the t_{2g} and from 13% to 11% for the t_{2g}^*. This effect is even more pronounced for the e_g^* (from 52% to 38%).

Table 1: Composition of occupied and unoccupied MOs originating from the iron 3d AOs in clusters of $K_4[Fe(CN)_6]$ and Fe-(μCN)$_6$-Th$_6$-δ^-_x.

		Fe3*d* (%)	CN2π (%)	CN5σ (%)	Th5*f*/6*d* (%)
$K_4Fe(CN)_6$ MOs	$\mathbf{e_g}$	18	-	82	-
	$\mathbf{t_{2g}}$	72	28	-	-
	$\mathbf{e_g^*}$	52	-	48	-
	$\mathbf{t_{2g}^*}$	13	87	-	-
Fe-(μCN)$_6$-Th$_6$-δ^-_x MOs	$\mathbf{e_g}$	14	-	86	-
	$\mathbf{t_{2g}}$	67	27	-	6
	$\mathbf{e_g^*}$	38	-	53	9
	$\mathbf{t_{2g}^*}$	11	71	-	18

Table 2: Charges and electronic populations obtained by DFT from Mulliken and NPA methods. The results for the $K_4[Fe(CN)_6]$ cluster are shown in *italics* and the results for the Fe-(μCN)$_6$-Th$_6$-δ^-_x unit are shown in **bold**.

	charges		s electrons		p electrons		d electrons		f electrons	
	Mulliken	*NPA*	*Mulliken*	*NPA*	*Mulliken*	*NPA*	*Mulliken*	*NPA*	*Mulliken*	*NPA*
Fe	**-0.63**	**-0.31**	**6.40**	**6.43**	**13.36**	**12.01**	**6.84**	**7.88**	**0.02**	**0.00**
	-0.37	*-0.48*	*6.21*	*6.38*	*13.21*	*12.01*	*6.93*	*8.10*	-	-
C	**0.21**	**0.41**	**3.36**	**3.17**	**2.34**	**2.41**	**0.07**	**0.00**	**0.00**	**0.00**
	-0.06	*0.07*	*3.34*	*3.18*	*2.65*	*2.71*	*0.07*	*0.02*	-	-
N	**-0.47**	**-0.78**	**3.54**	**3.53**	**3.90**	**4.25**	**0.03**	**0.01**	**0.01**	**0.00**
	-0.44	*-0.62*	*3.69*	*3.58*	*3.70*	*4.01*	*0.05*	*0.02*	-	-
Th	**3.70**	**3.76**	**11.97**	**12.00**	**29.94**	**30.00**	**30.17**	**30.09**	**14.21**	**14.15**

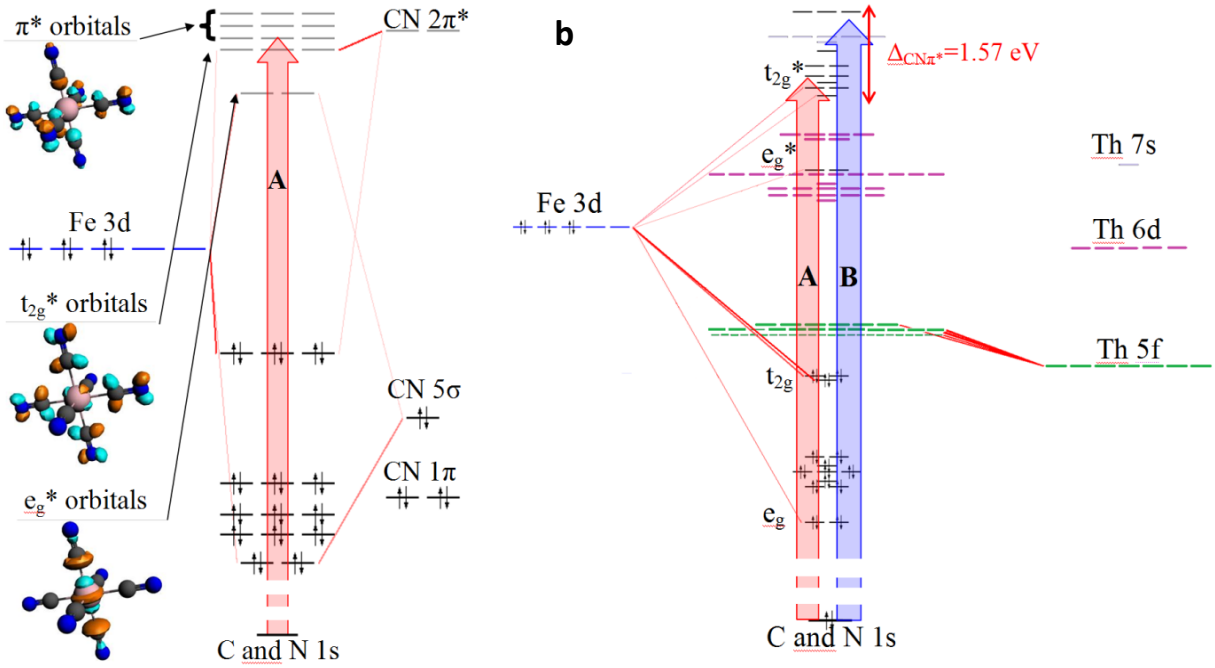

Figure 3: Molecular orbital diagrams calculated by DFT. **a)** $K_4[Fe(CN)_6]$ interactions between Fe^{2+} and CN^- fragments also showing vacant MOs involved in the XAS process (e_g*, t_{2g}*, and π*). **b)** Molecular orbital diagram for the Fe-$(\mu CN)_6$-Th_6-δ^-_x interaction.

c XAS simulation

Simulation of the XAS spectra represents an important step to corroborate experimental and theoretical data. Simulations were performed on the basis of the above DFT-calculated electronic populations (Mulliken), and DFT optimized structures determined by EXAFS for **$K_4[Fe(CN)_6]$** and **Th^{IV}/Fe^{II}**, respectively. Simulated spectra were compared to the experimental spectra of **$K_4Fe(CN)_6$** and **Th^{IV}/Fe^{II}**.

- **$K_4[Fe(CN)_6]$:**

Figure 4a-b shows energy-shifted simulated and experimental spectra for the nitrogen and carbon K-edges of **$K_4Fe(CN)_6$**. Atomic positions and electronic populations were set from the DFT-calculated structure **of $K_4Fe(CN)_6$** and the associated Mulliken calculation (**Table 2**). At the carbon edge, two peaks (**K_1** and **K_2**) at high energy correspond to the potassium $L_{2,3}$-edges and were not taken into account. With this exception, the carbon K-edge features are in good agreement with the simulated spectra. The main features are well reproduced for the carbon edge, with good accuracy over the entire energy range. For the nitrogen edge, the first main peak at lower energy is also well reproduced, but the higher energy features are less accurate. The spectral shape at high energy was found to be very sensitive to the local geometry. For the N K-edge simulation, the cluster chosen became too approximate and the first nearest neighbours (K^+, water) were not taken into account. However, these are the first reliable spectra and simulation for ferrocyanide obtained using the carbon and nitrogen K edges. In **Figure 3a** the light blue, blue, and grey curves correspond to the calculated DOS of 2*p* character for the absorbing atom (nitrogen and carbon). The O 2*p* DOS exhibits 3 distinct types of 2*p* contributions associated with the MOs σ*, π* and t_{2g}*. The t_{2g}* and π* 2*p* DOS are convoluted over the first peak **A** (blue and light blue, respectively) and match the t_{2g}* and π* MOs derived from the DFT calculation. Although the iron-cyano π bonding is associated with orbital mixing (**Table 1**: 13% Fe 3*d* contribution), the corresponding t_{2g}* and π* split is too small to be observed experimentally.

- **Th^{IV}/Fe^{II}:**

Based on the methodology implemented for **$K_4[Fe(CN)_6]$**, the same monoelectronic approach was used to simulate the carbon and nitrogen edges of **Th^{IV}/Fe^{II}**. Atomic positions were set from previous EXAFS data and the electronic populations were obtained by DFT calculations for the Fe-$(\mu CN)_6$-Th_6-δ^-_x cluster presented above. The simulated XAS spectra obtained with Mulliken charges are compared to the experimental spectra in **Figure 5a-b**. Several other electronic configurations were tested and are included in **SI. 2**. At the nitrogen K-edge, peak **A** is well reproduced at 399.5 eV, whereas peak **B** at 401.5 eV is distorted and reproduced with lower intensity. At the carbon K-edge, the same trend can be observed. In both cases it is clear that the simulated peak energy positions are in better agreement with the experimental data than their relative intensities. This is particularly true at the carbon K edge, for which peak **B** is very small compared to that obtained experimentally. Moreover, better simulation accuracy was obtained for the nitrogen K-edge compared to carbon K-edge. This can be attributed to the radius used for simulations (5.0 Å): On the one hand, the cluster was N-centered for the N K edge calculation and the simulation provided a better description of the thorium environment (taking into account 6 coordinating cyano and and 3 water molecules), while on the other hand, the C-centered 5.0 Å cluster used to simulate the C K-edge only took into account 4 complete cyano and 2 water molecules. Overall, the simulated spectra are very satisfactory and can be used for interpretation with the help of corresponding DOS. The thorium 6*d* / 5*f* and iron 3*d* partial DOS are shown in **Figures 5a** and **5b**. These DOS are associated with MOs potentially involved in covalent bonding, according to the DFT calculations. First, the iron 3*d* DOS partially appears at the same energy as the first peak (**A**) and can be associated with the t_{2g}* MOs, as in **$K_4[Fe(CN)_6]$**. The 5*f* and 6*d* thorium DOS appear at the energy position coinciding with peak **B**.

This confirms that cyano π* splitting due to overlap with the thorium 6*d* and 5*f* AOs results experimentally in an increase of peak B at higher energy. This is consistent with the cyano π*/thorium 5*f*-6*d* mixing observed in DFT simulation for the Fe-$(\mu CN)_6$-Th_6-δ^-_x cluster. Briefly, the iron 3*d* and thorium 5*f* and 6*d* DOS analyses suggest that three types of π* orbitals can be identified over the two spectral peaks: 1) As for $K_4[Fe(CN)_6]$, the non-bonding π* and t_{2g}* which contribute to peak A; 2) At higher energy, the shifted π* MOs resulting from the covalent interaction between thorium and cyano ligands which contribute to peak B

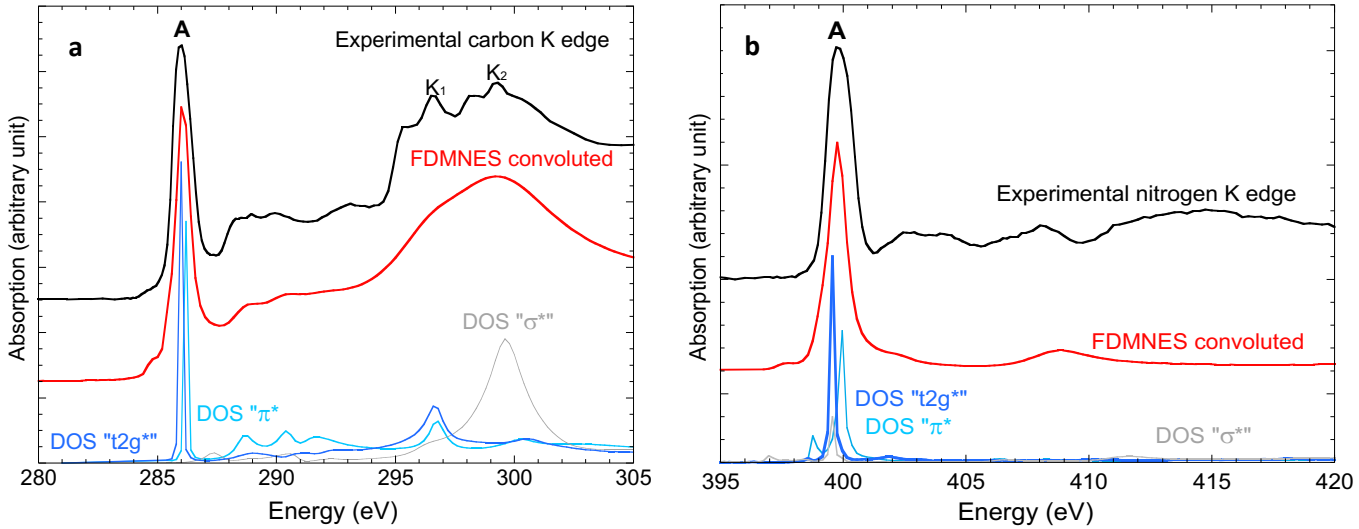

Figure 4: **a)** $K_4[Fe(CN)_6]$ nitrogen K-edge and simulation. **b)** $K_4[Fe(CN)_6]$ Carbon K edge, and simulation. Experimental spectra are shown in black and the simulated spectra in red. The 2p DOS attributed to t_{2g}*, π*, and σ* orbitals are blue, light blue, and gray, respectively.

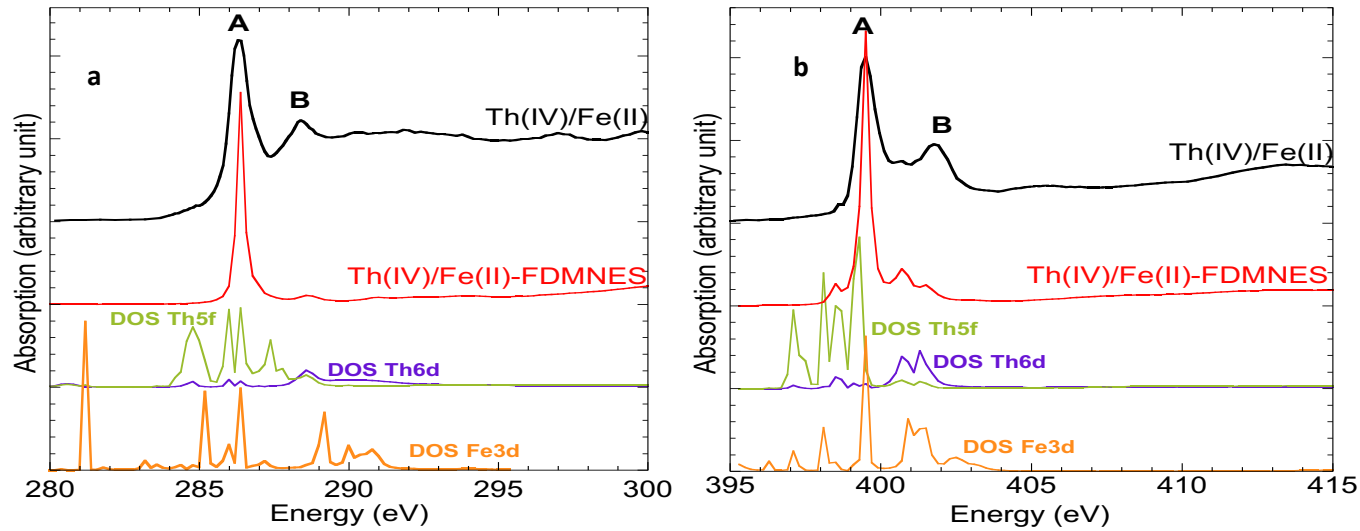

Figure 5: **a)** The $Th_6[Fe(CN)_6]$ nitrogen K-edge spectra and simulation. **b)** The $Th_6[Fe(CN)_6]$ carbon K-edge spectra and simulation. Experimental spectra are shown in black and the simulated spectra are red. The calculated thorium 5f and 6d DOS are green and violet, respectively, with the iron 3d DOS shown in orange.

C Discussion

From the above results, the following points may be noted for both iron/cyano and thorium/cyano bonding modes:

1) Fe-CN bond:

As mentioned above, the iron-cyano bond consists of σ-donation and π back-bonding. Considering the presence of a formal +4 and +3 charge on Th and Nd, respectively, Th and Nd are expected to make the cyano σ-donation to iron less effective and the π-back-bonding greater, *i.e.* to drive electrons from Fe to the Th/Nd atoms. The DFT results presented in **Table 2** are consistent with this image: the iron 3d electronic population (formally $3d^6$ for Fe^{2+}) rises to 6.93 eV in **$K_4[Fe(CN)_6]$** because of the σ-donation. Because of the Th^{4+} addition, the iron 3*d* electron population decreases to 6.84 eV for **Fe-(μCN)$_6$-Th$_6$-δ^-_x**. **Table 1** indicates a lower contribution from the 3d orbitals to the e_g MO (formed by the cyano/iron σ-donation): 18% for **$K_4[Fe(CN)_6]$** compared to 14% for **Fe-(μCN)$_6$-Th$_6$-δ^-_x**. On the contrary, the expected increase in the π-back-bonding effect was not observed. The π* contribution to the t_{2g} did not become significantly larger (28% and 27% for **$K_4[Fe(CN)_6]$** and **Fe-(μCN)$_6$-Th$_6$-δ^-_x,** respectively). The Fe-cyano π interaction is therefore hindered by π*/*5f-6d* contribution (6%) in t_{2g} MOs in the **Fe-(μCN)$_6$-Th$_6$-δ^-_x** cluster. Although phenomenological and limited by the experimental resolution (0.1 eV), the relative edge position in the series can be linked to the charge state of the absorbing atoms (*i.e.* the electron density for iron and cyano ligands). In fact, experimental energy shifts track the theoretical trend from **$K_4[Fe(CN)_6]$** to **Th^{IV}/Fe^{II}** in the following manner: at the N K-edge, C K-edge, and Fe L_3-edge the experimental energy shifts with respect to **$K_4[Fe(CN)_6]$** were -0.3 eV, -0.2 eV and 0.3 eV, respectively for **Th^{IV}/Fe^{II}**; and -0.2 eV, -0.3 eV and 0.2 eV respectively for **Nd^{III}/Fe^{II}**. This can therefore be considered as evidence of an increase in electronic density on cyano and a concomitant decrease in Fe when CN^- becomes a bonding ligand.

The Mulliken electronic structure confirms this trend. The decrease in the LMCT effect can be attributed to an attenuation of the σ-donation. Moreover, the MOs composition analyses highlight the influence of Th on the Fe-cyano π interaction. This interaction was further assessed by the experimental and theoretical description of the empty orbitals which follows.

1) Th-NC bond

Because a closed shell element is compulsory to perform the relevant simulations within the Fe-(μCN)$_6$-X$_6$-δ^-_x (X=Th, Nd) cluster model, no calculations were performed on the **Nd^{III}/Fe^{II}** compound. For this reason, the experimental XAS edge of the Nd compound is discussed compared to **K$_4$[Fe(CN)$_6$]** and **Th^{IV}/Fe^{II}**. The most noticeable change in the experimental carbon and nitrogen XAS spectra was the appearance of peak **B** in the **Th^{IV}/Fe^{II}** spectrum (indicated as feature **a** for **Nd^{III}/Fe^{II}**). This peak was attributed to π* orbital splitting based on the results of the following effects:

a) For **K$_4$[Fe(CN)$_6$]**, the iron/cyano π back-bonding did not affect the spectral shape, as shown by the DFT calculations (**Figure 2a**) and XAS simulations. It was demonstrated that the O 2*p* DOS attributed to cyano π* and t_{2g}* MOs are energetically too close to be experimentally resolved (**Figure 3a-b**). As a result, only a single absorption feature for **K$_4$[Fe(CN)$_6$]** (peak **A** on **Figure 1 a-b**) was observed.

b) For **Nd^{III}/Fe^{II}** and **Th^{IV}/Fe^{II}**, experimental XAS spectra show a second feature at higher energy (Nd: peak **a** at 1.5 eV after peak **A**; Th: peak **B** at 2.2 eV after peak **A**). These two peaks were assigned to a cyano π* splitting and attributed to a covalent interaction between Th (and to a lesser extent, Nd) and the cyano π* orbitals. This result was further confirmed by DFT calculations and XAS simulations performed for **Th^{IV}/Fe^{II}**. DFT results confirmed the splitting of the cyano π* orbitals arising from π* - 5*f* /6*d* orbital interactions. Red **A** and blue **B** arrows in **Figure 2** correspond to these two types of *1s*-2*p* transitions and were observed experimentally as peaks **A** and **B** in carbon and nitrogen K-edge spectra. With the help of the spectral simulations (**Figures 4a-b**), the *5f* and *6d* DOS contributions were observed at the same energy as peak **B**, and confirm the proposed assumption of a covalent interaction between the thorium 5*f*/6*d* and cyano π* MOs. Finally, the lower intensity of peak **a** compared to that of peak **B** could be evidence of the more effective π interactions of **Th^{IV}/Fe^{II}** compared to **Nd^{III}/Fe^{II}**. This is presumably due to the relatively smaller extension of the 4*f* and 5*d* orbitals and a correspondingly smaller effect on the cyano π* MOs.

More precise calculations would be required to describe the covalence effects more thoroughly. To avoid computational problems, simulations were performed with arbitrary charge configurations (**SI. 2**) but without any real improvement of the simulation efficiency. Geometrical effects were also tested (**SI. 4**) by varying the linearity of the cyano bridge. The energy position of peak **A** was unchanged with the deviation from linearity, but its intensity decreased. In contrast, peak **B** increased by bending the cyano bridge. This trend in the DOS simulation reveals the competition between Fe-CN and Th-NC orbital mixing and is further evidence of the proposed Th-5*f*,6*d*/cyano-π* interaction.

Conclusions

Combinations of NEXAFS experiments, DFT calculations, and NEXAFS spectral simulations at both the carbon and nitrogen K-edges were performed to describe the electronic structures of potassium, neodymium, and thorium ferrocyanide complexes.

To our knowledge, this is the first experimental work conducted at the ferrocyanide carbon and nitrogen K-edges that has combined with a semi quantitative approach. This methodology complete previous results on iron $L_{2,3}$-edge experiments for the ferrocyanide complexe. It provide for the first time consistent result from the ligand side of the complex that confirm the covalent nature in the iron cyano bonds. and paves the way for studding other inorganic compounds.

In order to unravel covalency effects in actinide molecular solids, this methodology was extended to the Prussian blue analogs of neodymium and thorium. Electronic structural differences were observed between the two isomorphous lanthanide and actinide compounds, $KNdFe^{II}(CN)_6{,}4H_2O$ and $ThFe^{II}(CN)_6{,}5H_2O$. The Th-CN bonding mode has been described compared to the electronic structure of the ferrocyanide anion. The electronic density displacement observed from iron to the cyano ligands was attributed to the electrostatic effect of the thorium and neodymium charge. From DFT calculations and X-ray spectroscopy semi quantitative analysis, there is further evidence of an additional covalency effect on the Th-CN bond. The simulations attributed additional peaks in the NEXAFS spectra to cyano π* and thorium 5*f* /6*d* orbital mixing. This experimental evidence observed at both carbon and nitrogen K edge is indicative of the more covalent nature of the Th-cyano bond. The DFT results also indicate the ability of An^{4+} to form π interactions with unoccupied cyano π* orbitals like *d* block elements.

The presented XAS experiment à carbon and nitrogen edges are consistent with previous studies stating, back bonding effects in the Fe-CN bond. It is moreover confirmed by the accurate XAS spectrum simulation based on theoretical models. To contribute to the actinide community effort to discriminate between actinide and lanthanide coordination modes, we focused on ferrocyanide interaction with neodymium and thorium. Again based on experimental cyano carbon and nitrogen NEXAFS spectra, and consistent with theoretical methods, it was demonstrated that the cyano ligand LUMO was strongly affected by its interaction with thorium while almost no effect was observed with neodymium.

Acknowledgements

This work was supported by CEA/DEN under the RBPCH Program of Basic Research in Chemistry and by the European IRSES program under the HEXANE project (number 2 30807). Work at the Advanced Light Source is supported by the Director, Office of Science, Office of Basic Energy Sciences; the Molecular Environmental Sciences Beamline 11.0.2 is supported by the Director, Office of Science, Office of Basic Energy Sciences, Division of Chemical Sciences, Geosciences, and Biosciences Condensed Phase and Interfacial Molecular Sciences program; and DKS is supported by the Director, Office of Science, Office of Basic Energy Sciences Division of Chemical Sciences, Geosciences, and Biosciences Heavy Element Chemistry Program; all of the U.S. Department of Energy at Lawrence Berkeley National Laboratory under Contract No. DE-AC02-05CH11231.

Notes and references

[a] *CEA, Nuclear Energy Division, Radiochemistry and Process Department, 30207 Bagnols-sur-Cèze, France.*
Email: thomas.dumas@cea.fr
[b] *Helmholtz Zentrum Dresden-Rossendorf, 01314 Dresden, Germany*
[c] *Chemical Sciences Division, Lawrence Berkeley National Laboratory, Berkeley, CA 94720, USA*
[d] *Advanced Light Source Division, Lawrence Berkeley National Laboratory, LBNL, Berkeley, CA 94720, USA*
[e] *University of Nice Sophia Antipolis, Nice Chemistry Institute, UMR 7272, 06108 Nice, France*

1. R. C. Mehrotra, P. N. Kapoor, and J. M. Batwara, *Coord. Chem. Rev.*, 1980, **31**, 67-91.
2. E. Glueckauf and H. A. McKay, *Nature*, 1950, **165**, 594–595.
3. K. Street, G. T. Seaborg, *J. Am. Chem. Soc.*, 1950, **72**, 2790–2792.
4. M. Dolg, *Encyclopedia of Computational Chemistry*, 1998, **2**, 1478–1486.
5. P. Thuéry, M. Nierlich, N. Keller, and M. Lance, *Acta Cryst. Section C*, 1995, **51**, 801-805.
6. R. Denning, *J. Physic. Chem. A*, 2007, **111**, 4125–4143.
7. J.G. Brennan, S.D. Stults, R.A. Andersen, and A. Zalkin, *Organometallics*, 1988, **7**,1329-1334.
8. L. Karmazin, M. Mazzanti, and J. Pécaut, *Chem. Commun.*, 2002, **6**, 654-655.
9. M. Mazzanti, R. Wietzke, J. Pécaut, and J.M. Latour, *Inorg. Chem.*, 2002, **41**, 2389-2399.
10. K. Ingram, M.J. Tassell, A.J. Gaunt, and N. Kaltsoyannis, *Inorg. Chem.*, 2008, **47**, 7824-7833.
11. A. Gaunt, S. D. Reilly, J.A. Ibers, P. Sekar, K. Ingram, and N. Kaltsoyannis, *Inorg. Chem.*, 2008, **47**, 29-41.
12. A. Zaiter, B. Amine, Y. Bouzidi, L. Belkhiri, A. Boucekkine, and M. Ephritikhine, *Inorg. Chem.*, 2014, **53**, 4687–4697.

13. D. D. Schnaars, A. J. Gaunt, T. W. Hayton, M. B. Jones, I. Kirker, N. Kaltsoyannis, I. May, S. D. Reilly, B. L. Scott, and G. Wu, *Inorg. Chem.*, 2012, **51**, 8557–8566.
14. Q.-R. R. Huang, J. R. Kingham, and N. Kaltsoyannis, *Dalton. Trans.*, 2015, **44**, 2554–2566.
15. S. A. Kozimor, P. Yang, E. R. Batista, K. S. Boland, C. J. Burns, D. L. Clark, S. D. Conradson, R. L. Martin, M. P. Wilkerson, and L. E. Wolfsberg, *J. Am. Chem. Soc.*, 2009, **131**, 12125–12136.
16. S. G. Minasian, J. M. Keith, E. R. Batista, K. S. Boland, D. L. Clark, S. D. Conradson, S. A. Kozimor, R. L. Martin, D. E. Schwarz, D. K. Shuh, G. L. Wagner, M. P. Wilkerson, L. E. Wolfsberg, and P. Yang, *J. Am. Chem. Soc.*, 2012, **134**, 5586–5597.
17. S.G. Minasian, J.M. Keith, E.R. Batista, and KS Boland, *Chem. Sci.*, 2014, **5**, 351-359.
18. M. W. Loble, J. M. Keith, A. B. Altman, S. C. Stieber, E. R. Batista, K. S. Boland, S. D. Conradson, D. L. Clark, J. Lezama Pacheco, S. A. Kozimor, R. L. Martin, S. G. Minasian, A. C. Olson, B. L. Scott, D. K. Shuh, T. Tyliszczak, M. P. Wilkerson, and R. A. Zehnder, *J. Am. Chem. Soc.*, 2015, **137**, 2506–2523.
19. B. Hedman, K. Hodgson, and E. Solomon, *J. Am. Chem. Soc.*, 1990, **112**, 1643-1645.
20. S. Shadle, B. Hedman, K. Hodgson, and E. Solomon, *Inorg. Chem.*, 1994, **33**, 4235-4244.
21. S. Shadle, J. Penner-Hahn, H. Schugar, B. Hedman, K. Hodgson, and E. Solomon, *J. Am. Chem. Soc.*, 1993, **115**, 767-776.
22. R. K. Hocking, E. C. Wasinger, F. M. de Groot, K. O. Hodgson, B. Hedman, and E. I. Solomon, *J. Am. Chem. Soc.*, 2006, **128**, 10442–10451.
23. M. Arrio, P. Sainctavit, C. Moulin, T. Mallah, M. Verdaguer, E. Pellegrin, and C. Chen, *J. Am. Chem. Soc.*, 1996, **118**, 6422-6427.
24. C. Moulin, F. Villain, A. Bleuzen, M.-A. Arrio, P. Sainctavit, C. Lomenech, V. Escax, F. Baudelet, E. Dartyge, J.-J. Gallet, and M. Verdaguer, *J. Am. Chem. Soc.*, 2000, **122**, 6653-6658.
25. E. Coronado, M. C. Giménez-López, T. Korzeniak, G. Levchenko, F. M. Romero, A. Segura, V. García-Baonza, J. C. Cezar, F. M. de Groot, A. Milner, and M. Paz-Pasternak, *J. Am. Chem. Soc.*, 2008, **130**, 15519–15532.
26. M. Robin, *Inorg. Chem.*, 1962, **1**, 337-342.
27. C. Avendano, M. G. Hilfiger, A. Prosvirin, C. Sanders, D. Stepien, and K. R. Dunbar, *J. Am. Chem. Soc.*, 2010, **132**, 13123–13125.
28. D. Visinescu, C. Desplanches, I. Imaz, V. Bahers, R. Pradhan, F. A. Villamena, P. Guionneau, and J.-P. P. Sutter, *J. Am. Chem. Soc.*, 2006, **128**, 10202–10212.
29. T. Dumas, M. Charbonnel, I. Charushnikova, S. Conradson, C. Fillaux, C. Hennig, P. Moisy, S. Petit, A. Scheinost, D. Shuh, T. Tyliszczak, and C. Auwer, *New J. Chem.*, 2013, **37**, 3003–3016.
30. G. Dupouy, I. Bonhoure, S. Conradson, T. Dumas, C. Hennig, C. Naour, P. Moisy, S. Petit, A. Scheinost, E. Simoni, and C. Auwer, *Eur. J. Inorg. Chem.*, 2011, **2011**, 1560–1569.
31. C. Fillaux, J.C. Berthet, S. Conradson, P. Guilbaud, D. Guillaumont, C. Hennig, P. Moisy, J. Roques, E. Simoni, D. Shuh, T. Tyliszczak, I. Castro-Rodriguez, and C. Den Auwer, *C. R. Chimie.,* 2007, **10**, 859-871.
32. C. Fillaux, D. Guillaumont, J.-C. C. Berthet, R. Copping, D. K. Shuh, T. Tyliszczak, and C. Den Auwer, *Phys. Chem. Chem. Phys.*, 2010, **12**, 14253–14262.
33. H. J. Nilsson, T. Tyliszczak, R. E. Wilson, L. Werme, and D. K. Shuh, *Anal. Bioanal. Chem.*, 2005, **383**, 41–47.
34. T.Tyliszczak, A.P. Hitchcock, A.L.D. Kilcoyne, H. Ade, S. Fakra, W.F. Steele, and T. Warwick, *Rev. Sci. Instrum.*, 2002, **73**, 1591.
35. U. Ryde, M.H.M. Olsson, and K. Pierloot, *Theor. Comput. Chem.*,2001, **9**, 1-55.
36. G. te Velde, F.M. Bickelhaupt, E.J. Baerends, C.F. Guerra, S.J.A. van Gisbergen, J.G. Snijders, and T. Ziegler, *J. Comput. Chem.*, 2001, **22**, 931-967.
37. E. van Lenthe, A. Ehlers, and E.J. Baerends, *J. Chem. Phys.*, 1999, **110**, 8943-8953.
38. E.D. Glendening, J.K. Badenhoop, and F. Weinhold, *J. Comput. Chem.*, 1998, **19**, 628-646.
39. S. Bonhommeau, N. Ottosson, W. Pokapanich, S. Svensson, W. Eberhardt, O. Björneholm, and E. Aziz, *J. Phys. Chem. B*, 2008, **112**, 12571-12574.
40. S. Bonhommeau, N. Pontius, S. Cobo, L. Salmon, F. M. de Groot, G. Molnár, A. Bousseksou, H. A. Dürr, and W. Eberhardt, *Phys. Chem. Chem. Phys.*, 2008, **10**, 5882–5889.
41. Y. Joly, *Phys. Rev. B*, 2001, **63**, 125120.